ARTICLE

Tracking high-valent surface iron species in the oxygen evolution reaction on cobalt iron (oxy)hydroxides

Received 00th January 20xx,
Accepted 00th January 20xx

DOI: 10.1039/x0xx00000x

Seunghwa Lee,[a] Aliki Moysiadou, [a] You-Chiuan Chu, [b] Hao Ming Chen, [b] and Xile Hu *[a]

The oxygen evolution reaction (OER) is the bottleneck reaction of water splitting, which can be used to generate green hydrogen from renewable electricity. Cobalt iron oxyhydroxides ($CoFeO_xH_y$) are among the most active OER catalysts in alkaline medium. However, the active sites of these catalysts remain unclear. Here we use *operando* ultraviolet-visible (UV-Vis), X-ray absorption, and Raman spectroscopy to reveal oxidations of both Fe and Co ions in $CoFeO_xH_y$ during OER. By analyzing samples with different Fe contents and thickness, we find that the concentration of Fe^{4+} species at the surface, but not the concentration of Co^{4+} in the bulk, scales with the catalytic activity. These results indicate an Fe^{4+}-containing active site in $CoFeO_xH_y$.

Introduction

Hydrogen is a promising energy carrier for future sustainable energy systems.[1, 2] Water electrolyzers can produce green hydrogen using renewable electricity, but a substantial overpotential is required for the oxygen evolution reaction (OER) at the anodes of these devices, leading to energy loss. A tremendous amount of effects have been devoted to the development of OER catalysts composed of Earth-abundant elements.[3-6] Among them are cobalt (Co)-based materials including Co phosphate composites, (oxy)hydroxides, a variety of oxides and chalcogenides.[7-12] It has been shown that iron (Fe)-incorporated Co (oxy)hydroxides are among the best OER catalysts.[6, 8, 9]

Despite considerable efforts to investigate the roles of Co and Fe ions in CoFe oxides and (oxy)hydroxides,[3, 4, 8, 9, 12-21] conflicting experimental observations and explanations remain. Some studies reported Co^{3+} species[16, 17, 20] while others reported Co^{4+} species[15, 22] as the resting species at OER potentials; some studies showed evidence for Fe^{3+} to Fe^{4+} oxidation[17, 18] while others indicated no oxidation of Fe^{3+} in OER.[16, 20] These discrepancies make it difficult to understand the mechanism of Co- and Fe-containing OER catalysts. Most of these studies employed X-ray absorption spectroscopy (XAS) to probe the oxidation states of Co and Fe ions. Because XAS is a bulk technique and gives averaged information over the entire sample, it might not reveal minority species at the surface of a material which are responsible for the catalytic activity. Therefore, it is necessary to study the catalysts using techniques complementary to XAS. Moreover, measurements should be made to catalysts of different size to probe both surface and bulk species.

Herein, we combine *operando* ultraviolet-visible (UV-Vis), X-ray absorption and Raman spectroscopy to probe the nature of catalytic active sites in CoFe (oxy)hydroxides ($CoFeO_xH_y$). We obtained spectral features corresponding to both Fe and Co oxidations, and unraveled their different relevance to catalysis. By analyzing samples with different Fe contents and thickness, we identified oxidized Fe species at the surface that are essential to the activity of the catalyst. The correlation of surface Fe species with catalytic activity enhances the understanding of this promising OER catalyst.

Results and discussion

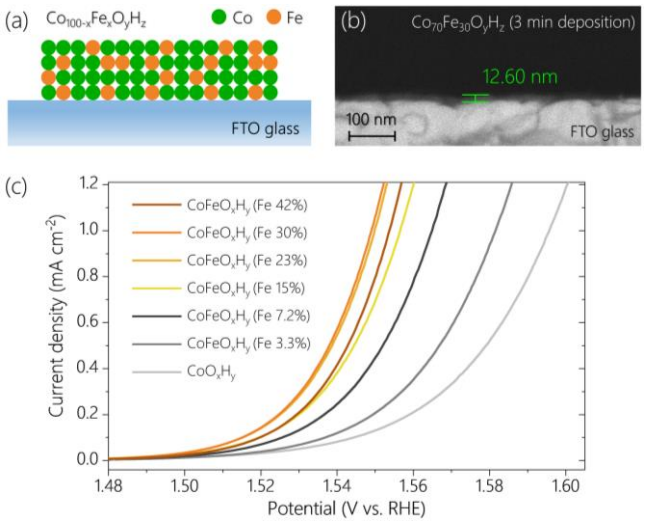

Figure 1. (a) A schematic presentation of $Co_{100-x}Fe_xO_yH_z$ on a FTO glass. (b) A representative SEM image of $CoFeO_xH_y$ film (30% Fe). (c) Linear-sweep voltammograms of the samples with various Fe contents recorded at a scan rate of 1 mV s^{-1} in Fe-free 0.1 M KOH

[a] *Laboratory of Inorganic Synthesis and Catalysis, Institute of Chemical Sciences and Engineering, ISIC-LSCI, École Polytechnique Fédérale de Lausanne (EPFL) 1015 Lausanne, Switzerland.*
[b] *Department of Chemistry, National Taiwan University, Taipei 10617, Taiwan.*
† Footnotes relating to the title and/or authors should appear here.
Electronic Supplementary Information (ESI) available: [details of any supplementary information available should be included here]. See DOI: 10.1039/x0xx00000x

$CoFeO_xH_y$ films with different Fe contents were prepared on fluorine doped tin oxide (FTO) glass by anodic electrodeposition.[23] The Fe contents varied from 0% to 42% (See Table S1), confirmed by inductively coupled plasma optical emission spectrometry (ICP-OES). By controlling the deposition time the total amount of metal ions was set to be similar for all samples (Table S1). Scanning electron microscope (SEM) images (Figures 1b and S1) indicate that the thicknesses of CoO_xH_y and $CoFeO_xH_y$ (Fe 30%) films deposited for 3 min were around 23.8 nm and 12.6 nm, respectively. The thicknesses of the different Fe-containing samples (deposited for 40-70 sec at the same anodic current density of 55.6 μA cm^{-2}, Table S1 and Figure S2) subjected to subsequent electrochemical tests (Figures 1c and S3) were estimated to be 4-5 nm.

The OER activity of the samples containing 0% to 42% Fe was measured by linear sweep voltammetry (LSV) at a scan rate of 1 mV sec^{-1} in Fe-free 0.1 M KOH (Figure 1c). As the Fe content increased up to 30%, the OER activity increased, consistent with earlier studies.[8, 16, 18, 24] The addition of Fe had also a significant effect on the Tafel slopes (Figure S3). The slope of Fe-free CoO_xH_y was about 52 mV dec^{-1}. The slope rapidly decreased to about 36 mV dec^{-1} at an Fe content of 7.2%, and only slightly changed at higher Fe content. The dramatic change in Tafel slope upon addition of Fe suggests a change of mechanism in OER.

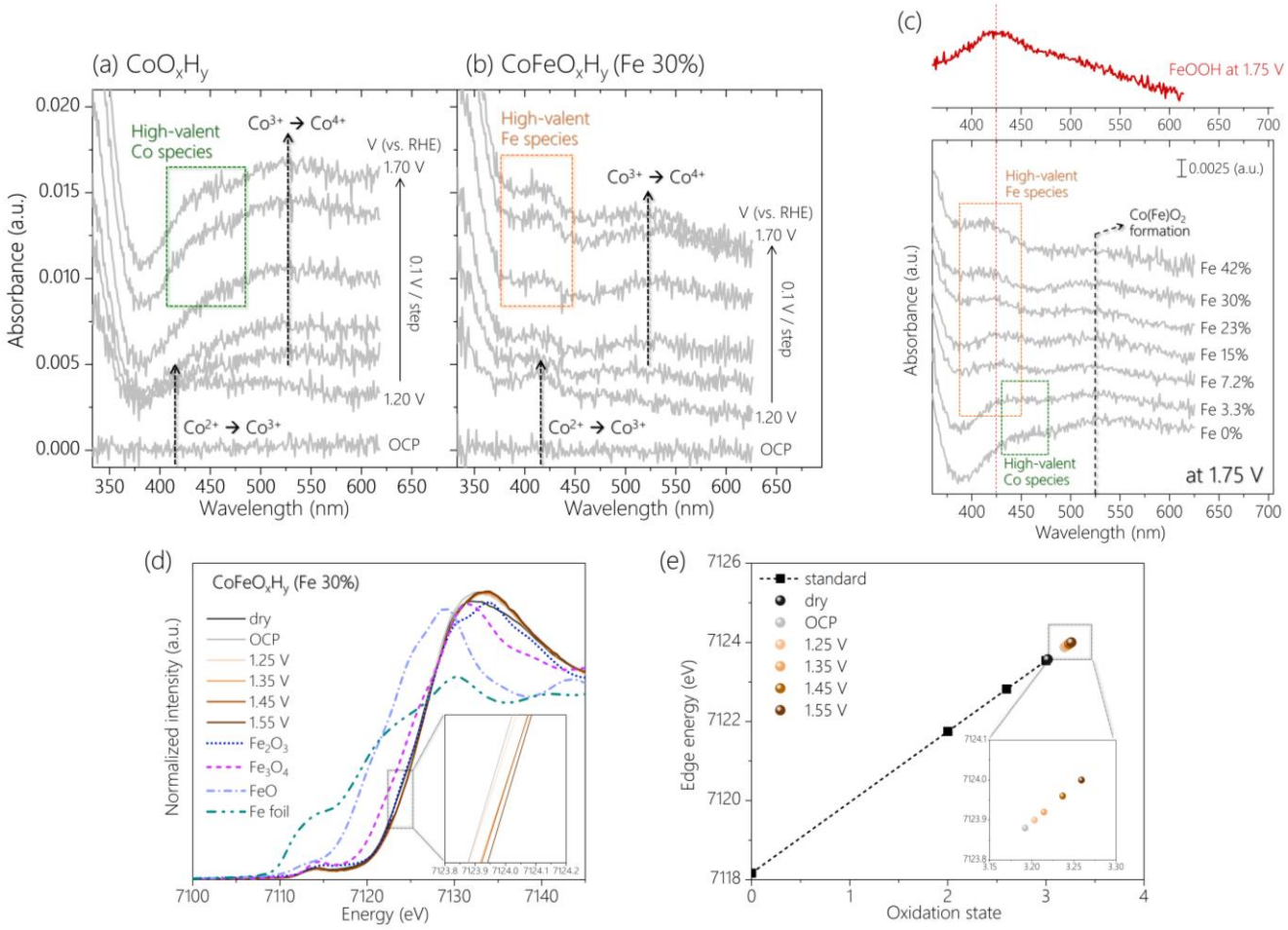

Figure 2. Operando UV-Vis spectra for (a) CoO_xH_y and (b) $CoFeO_xH_y$ (Fe 30%) obtained from OCP to 1.70 V with an interval of 0.1 V. (c) Operando UV-Vis spectra for the samples containing 0%, 3.3%, 7.2%, 15%, 23%, 30% and 42% Fe obtained at 1.75 V (vs. RHE). The reference spectrum of FeOOH is shown for comparison. (d) Operando Fe K-edge XANES spectra of $CoFeO_xH_y$ (Fe 30%) at various potentials compared to reference samples such as Fe foil, FeO, Fe_3O_4 and Fe_2O_3. (e) Correlation of edge energy with Fe oxidation state.

Operando UV-Vis spectroscopy (Figure S4) was employed to track changes in the oxidation states of Co and Fe sites. The spectra were obtained from open circuit potential (OCP) to 1.75 V with an interval of 0.05 V (Figure S5). Control experiments identified spectral features of a bare FTO substrate and an Fe oxyhydroxide film (FeOOH) in the OER potential region (Figure S6). The potential-dependent spectra of two representative samples, CoO_xH_y and $CoFeO_xH_y$ (Fe 30%) are depicted in Figures 2a and b. When the potential increased from OCP up to 1.20 V, a peak appeared at around 420 nm for both samples, which is attributed to the oxidation of Co^{2+} to Co^{3+}.[25] At 1.30 V and above, a broad spectral feature at around 525 nm was visible. A similar peak was reported in an earlier study, which assigned it to the oxidation of Co^{3+} to Co^{4+}.[25] If this is the case, CoO_xH_y is transformed to CoO_2.[22, 23, 26] Into the OER relevant potential region (>1.4 V), distinctive peaks were observed at 450 nm for CoO_xH_y and 425 nm for $CoFeO_xH_y$ (Fe 30%), respectively. We attribute the peaks to the accumulation of high-valent Co (450 nm) and Fe (425 nm) species (see below).

Comparison of the spectra for the samples at different Fe (Figure 2c) content under OER helps further clarify the spectral features. The peak at 525 nm (Co^{3+} to Co^{4+}) was visible in all

samples, suggesting the formation of Co^{4+} in both Fe-free and Fe-containing catalysts. Appropriate doping of Fe^{3+} ions was previously reported to promote the oxidation of Co^{3+} to Co^{4+},[19] while addition of a large amount of Fe^{3+} ions led to formation of phase-separated FeOOH.[8, 19, 27] Consistent with these reports and assuming the peak intensity on a per Co basis reflects the degree of oxidation to Co^{4+}, the UV-Vis data (Figure S7a) indicate a higher oxidation state of Co under oxidative conditions at a higher Fe content, up to 30% Fe. At an even higher Fe content, the peak intensity decreased due to the formation of inactive FeOOH species. The Fe-dependent formation of Co^{4+} is further supported by operando Raman spectra (Figure S8) and cyclic voltammograms (Figure S9) of CoO_xH_y and $CoFeO_xH_y$ (15% and 30% Fe). The formation of the $Co(Fe)O_2$ phase occurred at earlier potentials upon Fe doping.

The peak at 425 nm in the UV-Vis spectra (Figure 2c) was observed to grow with a higher Fe content, while the peak at 450 nm disappeared upon addition of Fe. Thus, the peak at 450 nm is due to the oxidation of Co species. This result is consistent with our previous study which showed that during OER on CoOOH the Co^{4+}-OH-Co^{4+} species was further oxidized to Co^{4+}-O·-Co^{4+} in a pre-equilibrium step.[23] Meanwhile, the UV-Vis spectrum of FeOOH at 1.75 V indicates that the 425 nm peak is due to the oxidation of Fe at higher potentials (>1.4 V). The intensity ratio of the peaks at 425 nm and 525 nm, denoted as A_{425nm}/A_{525nm} (Figure S7b), should correlate to the portion of oxidized Fe species relative to Co^{4+} in $CoFeO_xH_y$ during OER. This ratio increased with an increasing Fe content (Figures 2c and S7b). An abrupt increase of the ratio at 42% Fe is due to the formation of FeOOH. The correlation of A_{425nm}/A_{525nm} with activity up to 30% Fe suggests the oxidized Fe species is involved in OER.

Operando XAS was also performed to track the oxidation states of Co and Fe sites in the $CoFeO_xH_y$ (Fe 30%) during OER. Figure 2d displays the X-ray near edge absorption fine structure (XANES) for the Fe K-edge. A similar absorption energy to $Fe_2(III)O_3$ indicates the initial oxidation state of Fe ion as approximately +3. Upon immersion in the electrolyte, the Fe absorption edge was shifted to a higher energy, indicating that the Fe sites were slightly oxidized by the OH^- electrolyte. As the applied potential increased, the Fe absorption energy increases. This increase was quite distinctive at 1.45 V and above where OER begins to take place (see the inset in Figure 2d). To semi-quantitatively evaluate the Fe oxidation state during OER, the photon energies measured at half height at given potentials were extracted for linear fit with reference points (Figure 2e).[23, 28, 29] With higher applied potentials, the oxidation state of Fe ions gradually increased.[17] Their values were higher than +3.25 at 1.45 V and above, implying the presence of Fe^{4+} species under OER. This result agrees with the analysis of *operando* UV-Vis data. XAS also confirmed enhanced oxidation of Co^{3+} ions in $CoFeO_xH_y$ (Fe 30%) compared with that in CoO_xH_y XAS (Figure S10). The absorption edge of $CoFeO_xH_y$ kept shifting to a higher energy with increasing the applied potential, suggesting that the oxidation state of Co sites increased continuously. At 1.35 V, the corresponding oxidation state of Co in $CoFeO_xH_y$ was about +3.7, and it increased to about +3.9 at 1.55 V. For comparison, the oxidation state of Co ions in CoO_xH_y was about +3.4 at 1.55 V according to our previous work.[23]

Recently, it has been proposed that for certain OER catalysts the activation free energy decreases linearly with the amount of oxidative charge stored, which leads to a linear dependence of log(current density) on the surface coverage of active species.[30] We plotted log(current density) versus normalized absorbance of the UV-Vis peaks at 450 nm for CoO_xH_y and 425 nm for $CoFeO_xH_y$ (Fe 30%) (Figure 3). These peaks are assumed to represent the accumulation of high-valent Co and Fe species, respectively. We also plotted log(current density) versus normalized absorbance of the 525 nm, which represent Co^{4+} species. There are linear correlations between the log(current density) and the normalized absorbance of the UV-Vis peaks at 450 nm (for CoO_xH_y) and 425 nm (for $CoFeO_xH_y$), but not for the peak at 525 nm (for both CoO_xH_y and $CoFeO_xH_y$). The results might be explained by the following considerations: The Co^{4+} species in CoO_xH_y is further oxidized in OER and the concentration of the resulting species scales with activity. This result agrees with our previous study which showed that Co^{4+}-O·-Co^{4+}, formed by oxidation of Co^{4+}-O-Co^{4+}, was the resting species in the OER catalyzed by CoOOH.[23] Some bulk Co^{4+} are not oxidized[30-34] so that their concentration does not scale with activity. Upon Fe incorporation (>3.3%), a more active site

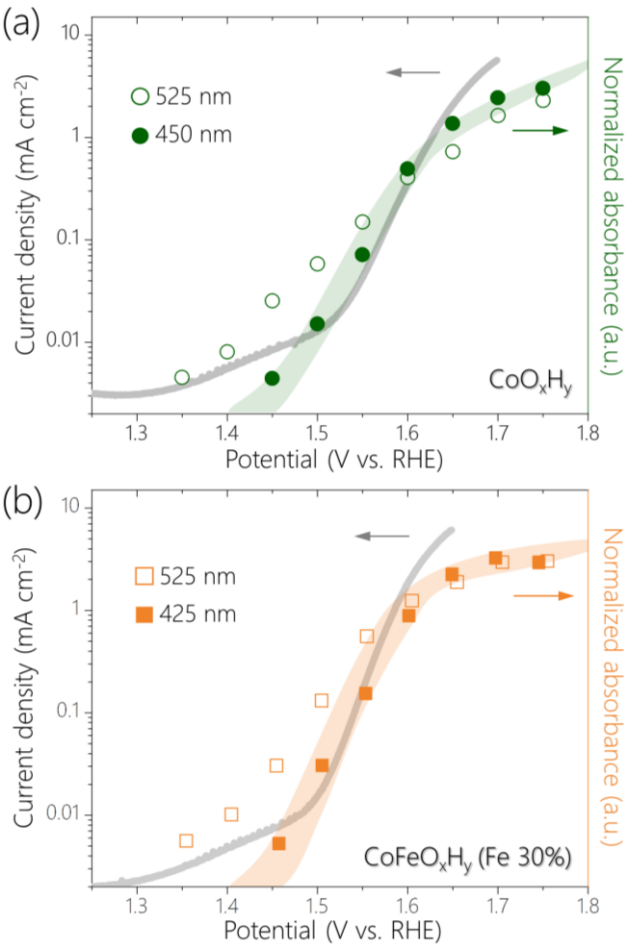

Figure 3. Tafel plots of (a) CoO_xH_y and (b) $CoFeO_xH_y$ (Fe 30%), overlaid with normalized absorbance at 450 and 525 nm for CoO_xH_y and 425 and 525 nm for $CoFeO_xH_y$. The features corresponding to the accumulation of high-valent Co (450 nm) and Fe (425 nm) follow the OER activity.

containing Fe (and likely also Co) is formed. The Fe^{3+} ions are oxidized and the concentration of the Fe^{4+} species scales with activity.

We hypothesize that the Fe-containing active sites in $CoFeO_xH_y$ are only located at the surface of the catalyst whereas Co^{4+} species are formed in the entire bulk (see Appendix 1). To verify the hypothesis, we studied $CoFeO_xH_y$ (30% Fe) with different thickness. The samples were prepared by varying the deposition time from 1 min to 6 min (Figure S11). Similar elemental compositions were confirmed by ICP-OES (Table S2). To estimate the electrochemical surface areas of the samples, their double-layer capacitance (C_{dl}) was acquired by cyclic voltammetry (CV) scans (Figures S12 and S13). The capacitance gradually deviated from a linear correlation with the amount of materials (deposition time), indicating that as the film grows thicker, an increasing portion of the bulk is not electrochemically active.

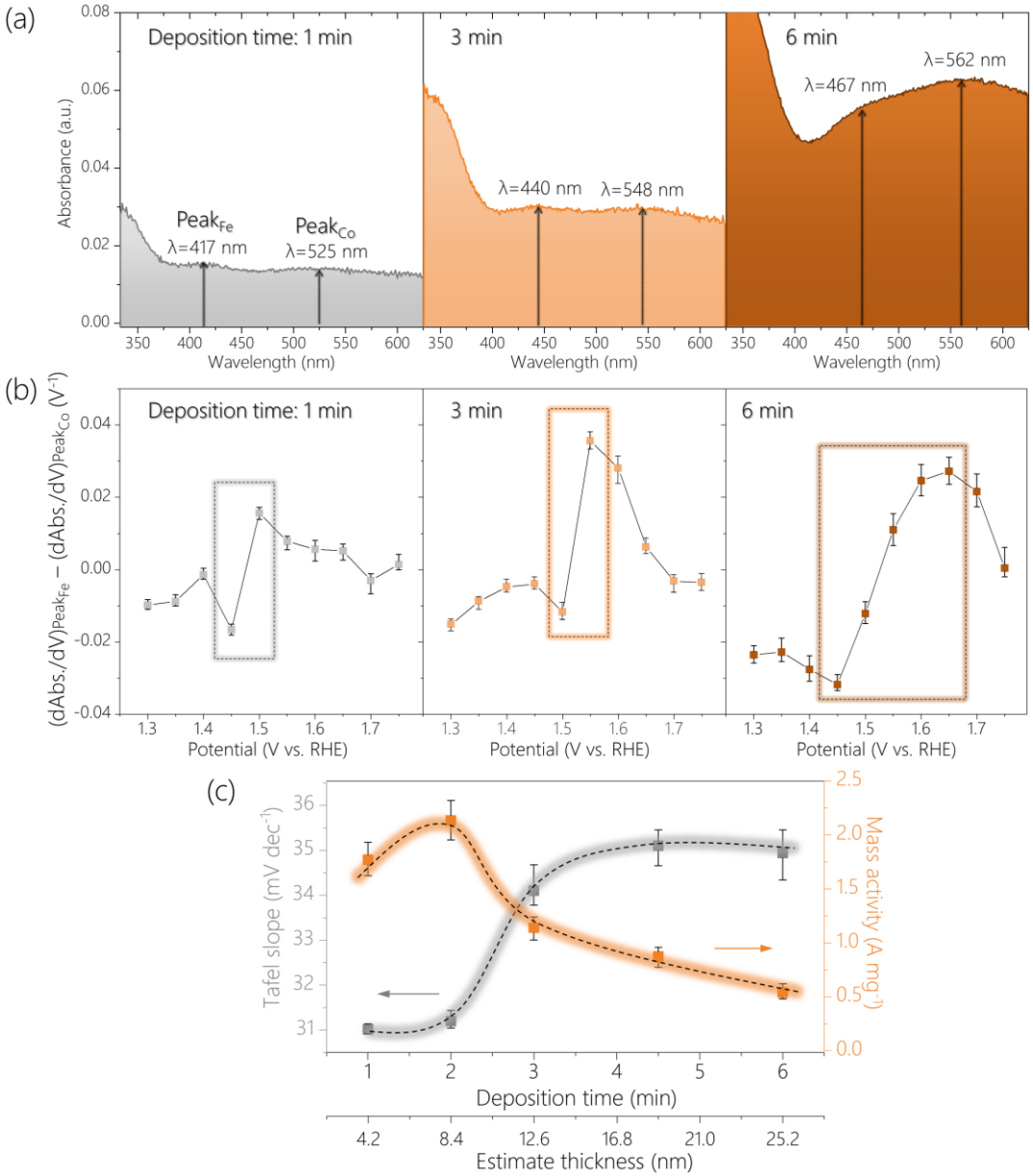

Figure 4. (a) Operando UV-Vis spectra of $CoFeO_xH_y$ (Fe 30%) films prepared at various deposition durations (1, 3 and 6 min) at 1.75 V (vs. RHE). (b) Difference in differential absorbance at 417, 440, 467 nm (for Fe^{4+}) and 525, 548, 562 nm (for Co^{4+}) for samples deposited at 1, 3 and 6 min as function of potential. (c) Comparison of Tafel slope and mass activity (at an overpotential of 340 mV) as function of deposition time and estimated film thickness.

The above $CoFeO_xH_y$ (Fe 30%) films were subjected to *operando* UV-Vis spectroscopy (Figures 4, S14 and S15) at applied potentials of 1.15 V to 1.75 V with an interval of 0.05 V in 0.1 M Fe-free KOH solutions. When the thickness of the film increased, the peaks corresponding to the Fe^{4+} and Co^{4+} species were shifted to longer wavelengths, from 417 nm to 467 nm and from 525 nm to 562 nm, respectively. These changes were attributed to thickness-related optical properties.[35-37] More importantly, the ratio of the absorption intensities for the Fe^{4+} and Co^{4+} (e.g., A_{417nm}/A_{525nm} for the 1 min-deposited sample) at 1.75 V gradually decrease from 1.14 to 0.91 upon increasing thickness (Figure S16). This result supports the hypothesis that only Fe

species at the surface are oxidized to +4 and the Co^{4+} species are distributed throughout a large part (if not all) of the bulk, as the proportion of the surface sites decreases when the film thickness increases. We studied CoO_xH_y films in different thicknesses, which again confirms the peak at higher wavelength (e.g., 525 nm for the 1 min-deposited sample) corresponds to the Co^{4+} species in the entire bulk (Figure S17).

To further compare the potential-dependent concentration of Fe^{4+} and Co^{4+} species, we plotted the differences in differential absorbance at the wavelength where these species absorb as function of potential according to a previously reported procedure (see Experimental methods) (Figures 4b and S18).[32] An upward spike was observed between 1.4 to 1.5 V for all samples, which coincided with the potential region where OER started to occur. This result is consistent with that catalytically relevant Fe^{4+} species are generated during OER but Co^{4+} species exist already before OER occurs. The thicker the film was, the higher the potential where the difference (dAbs./dV for Fe^{4+}-dAbs./dV for Co^{4+}) is at the maximum (see rectangular boxes in Figures 4b and S18). This result agrees with that Fe^{4+} species are at the surface and Co^{4+} species are at the bulk.

We analyzed the thickness dependence of electrocatalytic activity (Figure 4c). The Tafel slope was about 31 mV dec^{-1} for films of 4.2 nm and 8.4 nm, which increased to about 34 mV dec^{-1} for a film of 12.6 nm and increased further for thicker films. Meanwhile, total metal mass-based activity followed an opposite trend: best activity for films of 4.2 nm and 8.4 nm followed by continuous decrease at larger thickness. These results again support that the active sites are at the surface.

A previous study showed the optimal mass activity for OER on NiFe nanoparticles was obtained with samples of 5.4 nm.[33] Another work reported that the active species in sputtered films of NiO_x was accumulated only at the near surface (≤5 nm).[31] Even though these previous experimental results are from Ni-based materials it would be worth considering an optimal thickness of approximately 5-6 nm. To probe whether the active surface depth of $CoFeO_xH_y$ was also 5-6 nm, we prepared a $CoFeO_xH_y$ (Fe 30%) sample with a thickness of about 6.3 nm (Figures S19 and S20). This sample exhibited similar Tafel slope and spectroelectrochemical behavior but higher mass activity than samples of 4.2 and 8.4 nm. This result suggests the optimal thickness for electrodeposited metal oxyhydroxides is indeed about 5-6 nm.

Co oxides are reported for OER: spinel Co oxides[13, 38-42] and layered Co (oxy)hydroxides.[16-18, 22, 23] The Co ions in these two types of compounds have different geometries and coordination environments, so the mechanisms of OER are expected to be different as well. Previous studies of spinel Co oxides indicate that the resting state of Co is Co^{3+}, and doped Fe ions are not oxidized during OER.[16, 38-41] The role of Fe might be the promotion of Co active sites.[16, 19, 41] The electrochemical activity (e.g., Tafel slopes) and spectral features of spinel Co oxides are distinct from those of the Co (oxy)hydroxides reported here. These differences are understandable given their different structures.[16, 17, 19, 22, 23, 38-42] Note that spinel Co oxides might be unstable and transformed into Co (oxy)hydroxides during OER.[40, 43]

We compare our results to those of previous studies of electrochemically deposited CoFe OER catalysts. The active forms of these catalysts are likely CoFe (oxy)hydroxides, although exceptions might exist. The group of Yeo found only Co but not Fe oxidation in Fe-doped CoO_x by operando XAS.[20] Because the same spectral features but different activity are found for Co in CoO_x, CoO_x + Fe^{3+}, and $Fe_{48}Co_{52}O_x$, they suggested that Co was not the active site for Fe-containing catalysts. Based on the lowering of coordination number from 6 to 5.3, they proposed that the unsaturated Fe species are the active sites. Because the Fe ions were adsorbed on CoO_x by CV measurements of the latter in Fe-containing solutions, multiple Fe species might form. This possibility, coupled with the thickness of CoO_x being about 10 nm, might explain why no Fe oxidation was observed in their study.

On the contrary, the group of Boettcher observed XAS spectral features corresponding to Fe oxidation and Fe-O bond shortening but not those corresponding to Co oxidation during OER on electrochemically deposited thin-film CoFe (oxy)hydroxides.[17] Their observation of Fe oxidation agrees with our finding, but the lack of Co oxidation in their study contrasts with our data. On the other hand, many other studies of CoOOH-type catalysts reported the oxidation of Co^{3+} to Co^{4+} similar to our work.[22, 23, 25, 26] The group of Nocera detected Fe^{4+} species in $CoFeO_x$ films employing *ex-situ* zero-field ^{57}Fe Mössbauer spectroscopy and XAS.[18] It is not clear whether the active form of the catalyst has a spinel or layered structure, and whether Co^{3+} or Co^{4+} was the main Co species. The detection of Fe^{4+} species ex-situ (meaning at ocp) indicates such species are spectators instead of active sites in OER. The authors suggest these Fe^{4+} serve as a redox-cooperative center to promote a nearby Co active site. We suspect their materials to be quite different from ours because a significant change of Tafel slopes occurred only at high Fe content (>20%) in their samples, whereas in our samples an Fe content of about 7% already led to a dramatic decrease of Tafel slope. We note that the catalysts employed in the above studies were made by cathodic electrodeposition of Co nitrates, where reduction of nitrate gave OH^- ions that reacted with Co ions to form $Co(OH)_2$ species. These films might be quite heterogeneous in composition. On the other hand, our catalyst is deposited by anodic deposition, which is known to give ultrathin films.[44]

Dionigi et al. applied operando XAS and X-ray scattering spectroscopy as well as density functional theory calculations to study the mechanism of NiFe and CoFe layered double hydroxides (LDHs), which are crystalline reference for the amorphous mixed metal oxyhydroxides made by electrodeposition.[15] They provided the first experimental evidence of the OER-active γ-phase of the materials, transformed from the as prepared a-phase of LDHs. According to the calculations, the Ni and Co ions should be in the mixed +3 and +4 formal oxidation state, and the Fe ions should be in the +4 oxidation state or higher. This result agrees with our data. However, due to electrochemically inaccessible nano domains in catalyst films, phase transitions are typically incomplete under OER potentials. This incompleteness results in various weighted averages of +2, +3, and +4 for the oxidation states of

metal ions, which are reflected in the different results discussed above. By using ultrathin catalyst films and multiple operando spectroscopy, in this study we are able to differentiate the roles of various surface and bulk species.

Concerning the actual active site for $CoFeO_xH_y$, two possibilities are consistent with the spectral data: (i) Fe is the active site which is mostly likely connected to a Co site by a bridging O or OH ligand.[45, 46] According to the DFT calculations of Dionigi et al.,[15] the active site of CoFe LDH is Fe^{4+}-OH-Co^{4+}, and the OER occurs by deprotonation of the bridged OH with concomitant Fe oxidation. This mechanism is consistent with our data, so are catalytic cycles involving an Fe^{4+}=O. (ii) The active site is still Fe-OH-Co, but Co serves as the oxygen evolving center while Fe serves as the redox support. In this scenario, Fe replaces the role of a redox-active O ligand as proposed previously for the OER on Fe-free CoOOH.[23] It is difficult to experimentally differentiate the two possibilities, but DFT calculations can be used to compare their energetics. Most DFT computations seem to favor an Fe-based oxygen evolving site.[14, 15, 17, 24, 47, 48]

Conclusion

In summary, we applied *operando* UV-Vis, XAS, and Raman spectroscopy to investigate the oxidation of metal ions during OER on Co and CoFe (oxy)hydroxides (CoO_xH_y and $CoFeO_xH_y$). For both catalysts the oxidation of Co^{3+} to Co^{4+} occurs before the onset of OER. For CoO_xH_y, a Co-based oxidation was observed at the onset of OER. This oxidation is absent in OER on $CoFeO_xH_y$; instead, an Fe^{3+} to Fe^{4+} oxidation concomitant to OER was identified for the latter. The Fe^{4+} species are only formed at the surface layer of $CoFeO_xH_y$ while the Co^{4+} species are present in a large part of the bulk material. The concentration of Fe^{4+} but not Co^{4+} correlates with the OER activity. Thus, the role of Fe is not only to promote the oxidation of Co^{3+} to Co^{4+}, but more importantly, to form a new active site at the surface that has higher activity. The work suggests ultra-thin nanoscale metal oxyhydroxides of about 5 nm thickness will have optimal mass-based activity because all metal ions are accessible for the OER.

Experimental

Materials

Cobalt nitrate ($Co(NO_3)_2{\cdot}6H_2O$, ≥98%, Sigma-Aldrich), iron nitrate ($Fe(NO_3)_3{\cdot}9H_2O$, ≥ 98%, Sigma-Aldrich) and sodium acetate ($NaCH_3CO_2$, anhydrous, ≥99%, Sigma-Aldrich) were used for electrode preparation. Deionized water (18 MΩ) from Milli-Q® Ultrapure Water System (Millipore, Bedford, USA) was used in this work. Potassium hydroxide solutions (1 N KOH standard solution, Merck KGaA) were diluted for experiments. Fluorine-doped tin oxide (FTO) coated glass (2.3 mm thick and surface resistivity ~13 Ω/sq., Sigma-Aldrich) served as a conductive substrate.

Electrode preparation

CoO_xH_y and $CoFeO_xH_y$ films were prepared on FTO glass by anodic electrodeposition at a constant current density of 55.6 μA cm^{-2}.[23] Prior to deposition, the FTO glass was washed in a mixture of ethanol and acetone (1:1) using a sonicator. The deposition bath for cobalt (oxy)hydroxide contained 0.01 M $Co(NO_3)_2{\cdot}6H_2O$ and 0.1 M $NaCH_3CO_2$. For the deposition of cobalt-iron (oxy)hydroxide films, a solution containing 0.1 M $NaCH_3CO_2$, $Co(NO_3)_2{\cdot}6H_2O$ and $Fe(NO_3)_3{\cdot}9H_2O$ with different compositions (total 0.01 M) was used.

Characterization

Electrode compositions were determined by inductively coupled plasma optical emission spectrometry (ICP-OES, Nexlon 350, PerkinElmer). The catalyst-deposited FTO glass was immersed in 2% nitric acid (HNO_3) diluted from 65% HNO_3 (Merck) such that the catalyst film could be dissolved. The resulting HNO_3 solution was analyzed to reveal the amounts of Co and Fe ions. Film thickness was probed with a Gemini field-emission scanning electron microscope operating at 1–3 kV accelerating voltage. Secondary electrons were collected with an in-lens detector. Side-view images were taken to measure the thickness by viewing a cross-section of the catalyst layer on FTO glass.

Electrochemical tests

All electrochemical experiments were carried out in KOH solutions purified by a previously reported method to remove Fe impurity.[8, 23] First, 0.5–1.0 g of $Co(NO_3)_2{\cdot}6H_2O$ were dissolved in 5 mL of ultrapure water and then 20 mL of 0.1 M KOH was added to this solution. $Co(OH)_2$ precipitate formed, which was subsequently washed with ultrapure water three times via centrifugation and decanting. The resulting $Co(OH)_2$ precipitate was suspended in 50 mL of 1.0 M KOH. Afterward, the suspension was mechanically agitated overnight to absorb Fe impurities from the 1 M KOH solution. Electrochemical measurements were performed with a multichannel potentiostat / galvanostat (VSP, Bio-Logic) in a three-electrode system consisting of a Pt wire counter electrode and a homemade double junction Ag/AgCl electrode (saturated KCl, E(Ag/AgCl) = 0.197 V vs. NHE, normal hydrogen electrode) as reference electrode. IR drop was compensated at a rate 90% by default through a Bio-Logic EC-Lab software. The measurements were carried out in a polypropylene beaker or a Teflon cell to avoid influences of the trace Fe impurity from surface of glass beaker. Unless otherwise stated, the acquired electrochemical data were referred to reversible hydrogen electrode (RHE) scale by following equation:

$$E\ (V\ vs.\ RHE) = E\ (V\ vs.\ Ag/AgCl) + 0.197\ V + 0.0592 \times pH \quad \text{Eq. 1}$$

Operando ultraviolet–visible (UV-Vis) spectroscopy

The operando UV-Vis measurements were conducted with a Cary 60 UV-Vis spectrophotometer (Agilent Technologies) using a three-electrode system in a custom-made electrochemical

Teflon cell. Prior to use, the Teflon cell was washed with an acid solution to remove Fe impurities and other dirt. The catalyst-deposited FTO glass was assembled to the electrochemical cell and then placed in the sample compartment of the UV-Vis spectrometer such that the sample can be irradiated properly. At the OCP, a spectrum as a blank was recorded for automatic baseline correction. With that, subsequent operando spectroscopic measurements were performed at each constant potential. All the spectra were collected in the transmittance mode.

Following a previous study,[32] differential changes in absorbance ($dAbs./dV$) were obtained at the wavelengths assigned to Fe^{4+} and Co^{4+} (e.g., 417 nm for Fe^{4+} and 525 nm for Co^{4+} in the sample deposited during 1 min as shown in Figure 4a) for the $CoFeO_xH_y$ (Fe 30%) samples prepared at various deposition times. The dAbs. represents the difference in the absorbance at two consecutive potentials separated by 0.05 V. Hence, dV is 0.05 V. In the potential-dependent plots ($dAbs.\ for\ Fe^{4+}/dV - dAbs.\ for\ Co^{4+}/dV$), the positive peaks at OER relevant potentials (1.5-1.65 V) indicate the increases of Fe^{4+} versus Co^{4+}.

Operando X-ray absorption spectroscopy (XAS)

For operando XAS measurements, all of the experiments were carried out at BL 01C, NSRRC, Taiwan. Each spectrum was measured after the calibration of either Co or Fe foil to prevent the deviation of incident energy. The *operando* XAS measurements were conducted in the customized electrochemical cell composed of Kapton window, a working electrode, a Pt counter electrode, and an Ag/AgCl reference electrode as reported in our previous work.[23] In order to analyze the XANES results, the obtained spectra were processed in Athena software to perform standard normalization to exclude the influence of thickness, concentration and amplifier settings.

Operando surface enhanced Raman spectroscopy (SERS)

The experiments were carried out in a customized electrochemical Teflon cell using a Raman microscope (in Via Raman microscope, Renishaw).[49] Prior to experiments, the Teflon cell was rigorously washed with an acid solution to remove impurities and then washed with a mixture of acetone and ethanol. Consistent with the set-up for operando UV-Vis spectroscopy, a three electrode system was used, in which a Pt wire and a homemade double junction Ag/AgCl electrode served as counter and reference electrode respectively. A 63× water-immersed objective (Leica-Microsystems) was applied to operando spectroscopic measurements. For a strong surface-enhanced effect, the 785 nm laser was used with the laser power of ~1% at the grating of 1200 l mm^{-1}. Spectrum was calibrated prior to use based on the wavenumber of silicon, 520±0.5 cm^{-1}. During experiments, each spectrum was collected through 15 consecutive scans with 1 s exposure time per scan. We used an electrochemically roughened gold (Au) as a substrate to obtain the surface-enhanced effect.[23] First, the Au was mechanically polished with alumina powder (1 µm) and then sonicated several times in 1:1 mixture of ethanol and acetone and then in ultrapure water. The clean Au was subjected to 20 oxidation-reduction cycling between -0.28 and 1.22 V vs. Ag/AgCl in 0.1 M KCl solution, in which the potential was held for 10 sec at the negative limit and 5 sec at the positive limit. After the potential cycling, the Au surface was reduced for 5 min at a constant potential of -0.3 V. Finally, the resulting brownish Au surface was thoroughly rinsed with ultrapure water. CoO_xH_y and $CoFeO_xH_y$ films were deposited on the roughened Au as described above for operando Raman spectroscopy experiments.

Conflicts of interest

There are no conflicts to declare.

Acknowledgements

This work is supported by the European Research Council (No. 681292) and the Marie Skłodowska-Curie Fellowship (No. 838367) under the European Union's Horizon 2020 research. This study is also supported by the Ministry of Science and Technology, Taiwan (MOST 109-2628-M-002 -001 -RSP). The work is part of NCCR Catalysis, a National Centre of Competence in Research funded by the Swiss Naitonal Science Foundation.

Notes and references

1 B. A. Pinaud, J. D. Benck, L. C. Seitz, A. J. Forman, Z. Chen, T. G. Deutsch, B. D. James, K. N. Baum, G. N. Baum and S. Ardo, *Energy Environ. Sci.*, 2013, **6**, 1983-2002.
2 S. Chu and A. Majumdar, *Nature*, 2012, **488**, 294-303.
3 F. Song, L. Bai, A. Moysiadou, S. Lee, C. Hu, L. Liardet and X. Hu, *J. Am. Chem. Soc.*, 2018, **140**, 7748-7759.
4 N. T. Suen, S. F. Hung, Q. Quan, N. Zhang, Y. J. Xu and H. M. Chen, *Chem. Soc. Rev.*, 2017, **46**, 337-365.
5 B. M. Hunter, H. B. Gray and A. M. Müller, *Chem. Rev.*, 2016, **116**, 14120-14136.
6 L. Han, S. Dong and E. Wang, *Adv. Mater.*, 2016, **28**, 9266-9291.
7 M. W. Kanan and D. G. Nocera, *Science*, 2008, **321**, 1072-1075.
8 M. S. Burke, M. G. Kast, L. Trotochaud, A. M. Smith and S. W. Boettcher, *J. Am. Chem. Soc.*, 2015, **137**, 3638-3648.
9 J. Wang, W. Cui, Q. Liu, Z. Xing, A. M. Asiri and X. Sun, *Adv. Mater.*, 2016, **28**, 215-230.
10 J. Huang, J. Chen, T. Yao, J. He, S. Jiang, Z. Sun, Q. Liu, W. Cheng, F. Hu and Y. Jiang, *Angew. Chem.*, 2015, **127**, 8846-8851.
11 Y. Liu, H. Cheng, M. Lyu, S. Fan, Q. Liu, W. Zhang, Y. Zhi, C. Wang, C. Xiao and S. Wei, *J. Am. Chem. Soc.*, 2014, **136**, 15670-15675.
12 N. H. Chou, P. N. Ross, A. T. Bell and T. D. Tilley, *ChemSusChem*, 2011, **4**, 1566-1569.
13 S.-F. Hung, Y.-T. Chan, C.-C. Chang, M.-K. Tsai, Y.-F. Liao, N. Hiraoka, C.-S. Hsu and H. M. Chen, *J. Am. Chem. Soc.*, 2018, **140**, 17263-17270.
14 C. Feng, M. B. Faheem, J. Fu, Y. Xiao, C. Li and Y. Li, *ACS Catal.*, 2020, **10**, 4019-4047.
15 F. Dionigi, Z. Zeng, I. Sinev, T. Merzdorf, S. Deshpande, M. B. Lopez, S. Kunze, I. Zegkinoglou, H. Sarodnik, D. Fan, A. Bergmann, J. Drnec, J. F. Araujo, M. Gilech, D. Teschner, J. Zhu, W.-X. Li, J. Greely, B. R. Cuenya and P. Strasser, *Nat. Commun.*, 2020, **11**, 1-10.

16 R. D. Smith, C. Pasquini, S. Loos, P. Chernev, K. Klingan, P. Kubella, M. R. Mohammadi, D. Gonzalez-Flores and H. Dau, *Nat. Commun.*, 2017, **8**, 1-8.
17 L. J. Enman, M. B. Stevens, M. H. Dahan, M. R. Nellist, M. C. Toroker and S. W. Boettcher, *Angew. Chem. Int. Ed.*, 2018, **57**, 12840-12844.
18 N. Li, R. G. Hadt, D. Hayes, L. X. Chen and D. G. Nocera, *Nat. Commun.*, 2021, **12**, 1-6.
19 L. Zhuang, L. Ge, Y. Yang, M. Li, Y. Jia, X. Yao and Z. Zhu, *Adv. Mater.*, 2017, **29**, 1606793.
20 L. Gong, X. Y. E. Chng, Y. Du, S. Xi and B. S. Yeo, *ACS Catal.*, 2018, **8**, 807-814.
21 F. Yang, K. Sliozberg, I. Sinev, H. Antoni, A. Bähr, K. Ollegott, W. Xia, J. Masa, W. Grünert, B. R. Cuenya, W. Schuhmann and M. Muhler, *ChemSusChem*, 2017, **10**, 156-165.
22 J. Zhou, Y. Wang, X. Su, S. Gu, R. Liu, Y. Huang, S. Yan, J. Li and S. Zhang, *Energy Environ. Sci.*, 2019, **12**, 739-746.
23 A. Moysiadou, S. Lee, C.-S. Hsu, H. M. Chen and X. Hu, *J. Am. Chem. Soc.*, 2020, **142**, 11901-11914.
24 S. H. Ye, Z. X. Shi, J. X. Feng, Y. X. Tong and G. R. Li, *Angew. Chem. Int. Ed.*, 2018, **57**, 2672-2676.
25 M. Risch, F. Ringleb, M. Kohlhoff, P. Bogdanoff, P. Chernev, I. Zaharieva and H. Dau, *Energy Environ. Sci.*, 2015, **8**, 661-674.
26 D. Friebel, M. Bajdich, B. S. Yeo, M. W. Louie, D. J. Miller, H. S. Casalongue, F. Mbuga, T.-C. Weng, D. Nordlund, D. Sokaras, R. Alonso-Mori, A. T. Bell and A. Nilsson, *Phys. Chem. Chem. Phys.*, 2013, **15**, 17460-17467.
27 D. Friebel, M. W. Louie, M. Bajdich, K. E. Sanwald, Y. Cai, A. M. Wise, M. J. Cheng, D. Sokaras, T. C. Weng, R. Alonso-Mori, R. C. Davis, J. R. Bargar, J. K. Norskov, A. Nilsson and A. T. Bell, *J. Am. Chem. Soc.*, 2015, **137**, 1305-1313.
28 X. Yang, K. Takada, M. Itose, Y. Ebina, R. Ma, K. Fukuda and T. Sasaki, *Chem. Mater.*, 2008, **20**, 479-485.
29 D. K. Bediako, B. Lassalle-Kaiser, Y. Surendranath, J. Yano, V. K. Yachandra and D. G. Nocera, *J. Am. Chem. Soc.*, 2012, **134**, 6801-6809.
30 H. N. Nong, L. J. Falling, A. Bergmann, M. Klingenhof, H. P. Tran, C. Spöri, R. Mom, J. Timoshenko, G. Zichittella, A. Knop-Gericke, S. Piccinin, J. Pérez-Ramírez, B. R. Cuenya, R. Schlögl, P. Strasser, D. Teschner and T. E. Jones, *Nature*, 2020, **587**, 408-413.
31 S. Corby, M.-G. Tecedor, S. Tengeler, C. Steinert, B. Moss, C. A. Mesa, H. F. Heiba, A. A. Wilson, B. Kaiser, W. Jaegermann, L. Francàs, S. Gimenez and J. R. Durrant, *Sustain. Energy Fuels*, 2020, **4**, 5024-5030.
32 C. Baeumer, J. Li, Q. Lu, A. Y.-L. Liang, L. Jin, H. P. Martins, T. Duchoň, M. Glöß, S. M. Gericke, M. A. Wohlgemuth, M. Giesen, E. E. Penn, R. Dittmann, F. Gunkel, R. Waser, M. Bajdich, S. Nemsak, J. T. Mefford and W. C. Chueh, *Nat. Mater.*, 2021, **20**, 674-682.
33 C. Roy, B. Sebok, S. B. Scott, E. M. Fiordaliso, J. E. Sørensen, A. Bodin, D. B. Trimarco, C. D. Damsgaard, P. C. K. Vesborg, O. Hansen, I. E. L. Stephens, J. Kibsgaard and I. Chorkendorff, *Nat. Catal.*, 2018, **1**, 820-829.
34 B. S. Yeo and A. T. Bell, *J. Am. Chem. Soc.*, 2011, **133**, 5587-5593.
35 S. Agnihotri, S. Mukherji and S. Mukherji, *RSC Adv.*, 2014, **4**, 3974-3983.
36 A. Shafiqa, A. A. Aziz and B. Mehrdel, *J. Phys. Conf. Ser*. 2018, **1083**, 012040.
37 G. A. López-Muñoz, J. A. Pescador-Rojas, J. Ortega-Lopez, J. S. Salazar and J. A. Balderas-López, *Nanoscale Res. Lett.*, 2012, **7**, 1-6.
38 H.-Y. Wang, S.-F. Hung, H.-Y. Chen, T.-S. Chan, H. M. Chen and B. Liu, *J. Am. Chem. Soc.*, 2016, **138**, 36-39.
39 H.-Y. Wang, S.-F. Hung, Y.-Y. Hsu, L. Zhang, J. Miao, T.-S. Chan, Q. Xiong and B. Liu, *J. Phys. Chem Lett.,* 2016, **7**, 4847-4853.
40 L. Calvillo, F. Carraro, O. Vozniuk, V. Celorrio, L. Nodari, A. Russell, D. Debellis, D. Fermin, F. Cavani and S. Agnoli, *J. Mater. Chem. A*, 2018, **6**, 7034-7041.
41 S. F. Hung, Y. Y. Hsu, C. J. Chang, C. S. Hsu, N. T. Suen, T. S. Chan and H. M. Chen, *Adv. Energy Mater.*, 2018, **8**, 1701686.
42 A. Bergmann, E. Martinez-Moreno, D. Teschner, P. Chernev, M. Gliech, J. F. De Araújo, T. Reier, H. Dau and P. Strasser, *Nat. Commun.*, 2015, **6**, 1-9.
43 A. Bergmann, T. E. Jones, E. M. Moreno, D. Teschner, P. Chernev, M. Gliech, T. Reier, H. Dau and P. Strasser, *Nat. Catal.*, 2018, **1**, 711-719.
44 C. G. Morales-Guio, L. Liardet and X. Hu, *J. Am. Chem. Soc.*, 2016, **138**, 8946-8957.
45 J. Wang, X. Ge, Z. Liu, L. Thia, Y. Yan, W. Xiao and X. Wang, *J. Am. Chem. Soc.*, 2017, **139**, 1878-1884.
46 J. Wang, L. Gan, W. Zhang, Y. Peng, H. Yu, Q. Yan, X. Xia and X. Wang, *Sci. Adv.*, 2018, **4**, eaap7970.
47 X. Han, C. Yu, J. Yang, X. Song, C. Zhao, S. Li, Y. Zhang, H. Huang, Z. Liu and H. Huang, *Small*, 2019, **15**, 1901015.
48 M. B. Stevens, L. J. Enman, E. H. Korkus, J. Zaffran, C. D. Trang, J. Asbury, M. G. Kast, M. C. Toroker and S. W. Boettcher, *Nano Res*., 2019, **12**, 2288-2295.
49 S. Lee, K. Banjac, M. Lingenfelder and X. Hu, *Angew. Chem. Int. Ed.*, 2019, **58**, 10295-10299.

